

DEVELOPMENT OF A VECTOR MAGNETOMETER BASED ON ELECTROMAGNETICALLY INDUCED TRANSPARENCY IN ^{87}Rb ATOMIC VAPOR

A.M. TOYRYLA¹ and I. NOVIKOVA¹
The College of William and Mary, Williamsburg, VA

(Dated: 8 April 2022)

We present progress towards the development of an atomic magnetometer capable of accurate scalar and vector magnetic field measurements with high sensitivity and no need for external calibration. The proposed device will use the interaction between a bi-chromatic laser field and rubidium vapor to derive magnetic field strength and direction from measured amplitudes of Electromagnetically Induced Transparency (EIT) resonances. Since the proposed method requires precision control of light polarization, we observe the performance capabilities of a liquid crystal device to rotate the polarization of the laser field. Another goal in this project is to optimize and characterize EIT resonances by varying laser frequency, modulation strength, and polarization locking parameters to most precisely measure and accurately describe magnetic fields. Finally, we realize a method to derive field direction from comparisons of EIT resonance strengths. The work completed herein will inform the greater project's noise reduction, component manufacturing, and device refinement steps that aim to produce the first compact and unobtrusive vector magnetometer.

I. Introduction

The precise measurements of the magnitude and direction of a magnetic field have long been achievable, but the instruments and methods used are often inherently imperfect. Hall probes and search coils use Lorentz forces and magnetic induction to spatially dislocate electrons in metals to create measurable voltages indicative of magnetic field strength. Magneto-resistive sensors use spin-dependent tunneling through magnetic thin films and are more sensitive than Hall probes. The most sensitive magnetometers we have today are the superconducting quantum interference device (SQUID) and the atomic magnetometer; both take advantage of quantum effects to translate magnetic fields into measurable quantities¹.

Today, only atomic magnetometers are truly considered accurate as they rely on fundamental constants of nature like the atomic g -factor (measured with high accuracy for most atoms) and the bohr magneton. Other instruments rely too heavily on uncontrolled variables or material properties. However, many types of atomic magnetometers are scalar devices, sensitive only to the total magnetic field value, and cannot determine the vector components of a field, which is crucial information for a plethora of magnetometer applications in aircraft, spacecraft, geological surveys, positioning systems, and submarine vision². Many modifications to the atomic magnetometer have been implemented, but all attempts to date either degrade accuracy or apply an external field which can interfere with nearby sensors.

This thesis is a part of a longer-term project aimed to demonstrate a vector atomic magnetometer operating at Earth-like magnetic field and capable of measuring magnetic field strength with sub-picotesla precision. For these experiments we will rely on Rubidium-87 (^{87}Rb) atoms interacting with a bi-chromatic laser field whose frequency will be tuned to match two optical transitions in Rubidium atoms. Under these conditions have observed several spectrally narrow resonances in the laser transmission. This effect is called Elec-

tromagnetically Induced Transparency, or EIT, and is caused by quantum interference of the multiple excitation pathways of a valence electron in Rb atoms. The position of each resonance will allow us to precisely determine the magnitude of the external magnetic field, while the relative amplitudes of the peaks provide information regarding the orientation of this field with respect to the propagation direction and the polarization of the laser beam.

The unique advantage of this approach is that no external calibration is required, a drawback of other magnetometers; the magnetic field orientation will be measured relative to the laser light polarization and propagation vector. Contrasting with existing devices, this project will combine scalar accuracy, long-term stability, vector measurement capability, and the absence of interfering applied fields into a single sensing unit. In the future, such a unit could be manufactured as a compact, chip-scale device that would facilitate magnetic object measurement and location tracking.

My role in this project is the optimization of EIT resonances to provide maximally accurate and precise magnetic field measurements, as well as the evaluation of vector magnetometer performance. This work will ensure this magnetometer's stability and accuracy even in the presence of technical noise and component fluctuations.

II. Theory Overview

A. Coherent Population Trapping

The central concept for this magnetometer's operation is electromagnetically-induced transparency (EIT) made possible through coherent population trapping (CPT) in rubidium vapor. A laser can be set to emit light of a frequency which matches a resonance frequency of rubidium; the atom may absorb a photon and move into an excited state in this case, later emitting a photon and moving back into the ground energy state. If we employ a bi-chromatic laser such that it emits

two coherent frequencies of light, each matching a resonant frequency of rubidium, we may place the atom in a superposition state. The requirement for this state is that the difference between the each laser frequency and resonance frequency be about the same.

The superposition state is called a “dark state” because an atom in this state does not interact with light. Since atoms in the dark state cannot interact with the EM field, they have been “trapped” and CPT causes electromagnetically-induced transparency. The EM field passes through the Λ -system with near zero chance of absorption, meaning there is nearly 100% transmission. Around this pair of frequencies, transmission increases sharply, forming what will be referred to as an EIT peak.

B. Zeeman Shifts and Scalar Field Measurement

Several magnetic energy sub-levels exist in the ground state of the rubidium atom; this is called hyperfine splitting. The Zeeman effect serves to split these levels by an energy difference linearly proportional to the static magnetic field applied to the system, $\Delta E_m = m\hbar\gamma B$. Here m is the azimuthal quantum number, \hbar is the reduced Planck’s constant, B is the magnetic field strength, and γ is a constant. EIT peaks occur between Zeeman sublevels with $\Delta m = 0, \pm 1, \pm 2$, where Δm is the difference in m between two given levels.

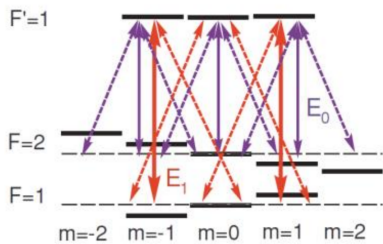


FIG. 1. Atomic levels in the $^{87}\text{Rb } 5S_{1/2} \rightarrow 5P_{1/2}$ optical transition, interacting with two EM fields E_0 and E_1 with frequencies ω_m separated by ground-state hyperfine splitting. Arrows represent possible transitions between Zeeman sublevels. The horizontal dashed lines indicate the unshifted positions of Zeeman sublevels. From reference³.

^{87}Rb has the energy level structure shown in Fig. 1 that allows for seven EIT peaks caused by CPT. They are separated in frequency from their neighboring peaks by $\Delta\nu = \gamma B$. Therefore, we arrive at a method to measure the magnetic field strength. The frequency separation of EIT peaks does not depend on the direction of the field, so this is a reliable method of measuring the scalar magnitude of any external magnetic field. An example of these EIT peaks found after a laser radio-frequency (RF) sweep is in Fig. 2.

Field direction affects the coupling strength between magnetic sublevels and therefore changes the amplitude of EIT peaks. Previous studies³, however, have demonstrated the existence of two permanent peaks corresponding to $a_{\pm 2}$ that do not disappear for any field orientation. When the magnetic

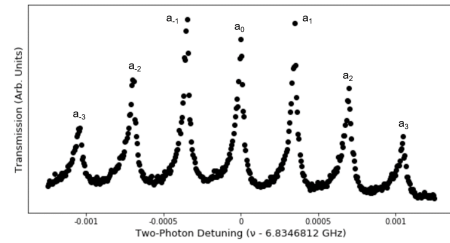


FIG. 2. Arrangement of seven EIT resonances evenly spaced in frequency $\Delta\nu = \gamma B$. Each is labeled a_n where n indicates the peak’s relative position to the central resonance, separated by $\Delta\nu = n\gamma B$. The frequency value in the x-label is the approximate frequency of the central resonance, 6.834 GHz.

field \vec{B} is parallel to the laser vector \vec{k} polarized at $\phi = 0^\circ$, quantum selection rules dictate that $\Delta m = 0$ transitions are allowed (the vertical arrows in Fig. 1); this restricts us to lambda da systems that are two levels off of hyperfine splitting, the $a_{\pm 2}$ peaks. These peaks can be used for reliable scalar field measurements.

C. Field Direction Measurement

The end of Section II B explains how EIT peaks change in amplitude based on the orientation of the magnetic field. This phenomenon presents a unique opportunity to measure the direction of the field without a need for external orientation calibration. The EIT resonance amplitudes depend on the relative orientations of three vectors: the laser wave-vector \vec{k} , the laser field polarization ϕ , and the magnetic field direction \vec{B} ^{4,5}. These three vectors are geometrically represented in Fig. 3.

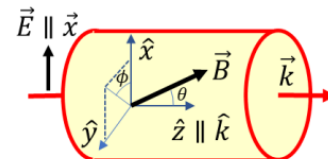


FIG. 3. Field geometry in the vapor cell. \vec{k} is the laser wave-vector, always oriented along the central axis of the vapor cell. \vec{B} is the magnetic field vector, an angle θ off of the \vec{k} vector. ϕ is the laser’s polarization, given as an angle relative to the plane formed by \vec{B} and \vec{k} . From reference³.

Transitions between energy levels with the same m (solid arrows in Fig. 1) are solely enabled by the laser polarization component along the magnetic field. Transitions between energy levels with $\Delta m = \pm 1$ (dashed arrows in Fig. 1) are solely enabled by the remaining orthogonal component. Theoretically, if we examine the possible two-photon transitions and all their combinations, we can calculate the resulting amplitude of each CPT resonance as a function of the angles between laser propagation, polarization, and the magnetic field direction vectors.

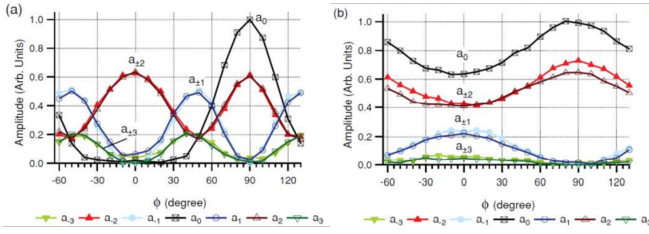


FIG. 4. Experimental Dependence of EIT resonance amplitudes on polarization angle ϕ in a magnetic field at angle (a) $\theta = 90^\circ$ and (b) $\theta = 15^\circ$ with respect to the laser wave-vector \vec{k} . Curves are labelled to match their corresponding EIT peak(s) in Fig. 2. From reference³.

Fig. 4(a) visualizes this dependence with experimental results³. It depicts a sweep of ϕ while the magnetic field is oriented at angle $\theta = 90^\circ$. The amplitudes for $a_{\pm 1}$ and $a_{\pm 3}$ are only nonzero when both polarization vector components parallel to and orthogonal to the \vec{B} field component in plane with polarization (the xy -plane in Fig. 3) are nonzero. The central peak a_0 has zero amplitude when polarization is parallel to \vec{B} 's polarization plane component. The peaks $a_{\pm 2}$, as discussed at the end of Section II B, always have nonzero amplitude, making them vital for measuring the scalar magnitude of the field in any direction.

We see that EIT peak amplitudes exhibit universal extrema whenever the light polarization is parallel or perpendicular to the magnetic field's polarization plane component. This forms an important basis for measuring magnetic field direction that is free from dependence on other experimental parameters like laser power. Thus, knowledge of the polarization direction ϕ and laser propagation direction \vec{k} can tell us about the azimuthal angle of the magnetic field if we compare the relative amplitudes of measured EIT resonance peaks.

In Fig. 4(b), the relative angle between the laser propagation \vec{k} and magnetic field direction \vec{B} has been reduced to $\theta = 15^\circ$. The overall variation in each of these amplitudes has decreased significantly. Once the \vec{B} field is parallel to the laser vector \vec{k} , each of these curves flattens entirely. Therefore, by measuring the variation in the amplitude of a single CPT resonance when ϕ changes, we can establish the angle θ between \vec{k} and \vec{B} .

With the scalar magnitude of the field established through the separation of EIT peaks, the azimuthal angle ϕ established through the relative amplitudes of the EIT peaks, and the angle θ between the magnetic field and laser propagation direction established through a resonance's response to changing polarization, this method fully characterizes any constant magnetic field vector \vec{B} .

III. Experimental Setup

The optics and electronics components complement each other for stable experimentation and measurement, but it helps to look at each separately for the full operational concept to be realized. In essence, a bi-chromatic laser with a frequency

locking mechanism first shines through a controllable polarization rotator. It then travels through a ^{87}Rb cell in a localized magnetic field, interacting with the atoms in a way dependent on the field conditions, and the remaining light arrives at a photodetector. The transmission data is read on a computer or oscilloscope and sent back through a feedback loop that locks the polarization rotator to the angle of peak transmission if desired.

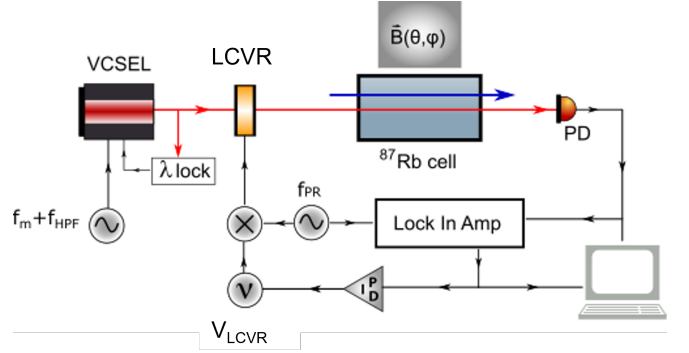


FIG. 5. Experimental Setup. VCSEL stands for vertical-cavity surface-emitting laser, the polarization rotator LCVR stands for Liquid Crystal Variable Retarder, V_{LCVR} is the voltage we send to the LCVR, f_{PR} is a modulation signal added on top of V_{LCVR} , PD is a photodetector, and the Lock-in Amplifier is a component of the feedback loop capable of derivative calculation.

A. Liquid Crystal Variable Retarder

The liquid crystal variable retarder (LCVR) is a key device of interest because its function is to rotate the plane of polarization of incoming light. In terms of the geometry of Fig. 3, this device changes ϕ , a key variable in determining magnetic field direction. The device performs the same function as a half-wave plate ($\lambda/2$), however it changes the angle at which it polarizes incoming light dependent on the voltage applied to it. This presents the opportunity to change ϕ to specific angles, sweep ϕ over its whole or partial range of possible values, and vary ϕ with a desired frequency.

Figure 6 shows a molecular cross-section of the LCVR. Applying no voltage to the device means all anisotropic nematic liquid crystal molecules are parallel to the fused silica and alignment layers. Maximum retardance is achieved in this state. An applied voltage will forcefully rotate and hold molecules in their rotated state so long as that constant voltage is applied. In the 0-10 V range the device is capable of taking in, higher voltages move the atoms towards being perpendicular to the alignment layer. The layer of molecules closest to each alignment layer are pinned, however, and are unable to rotate fully. Maximum and minimum retardance do not mean anything as metrics in this experiment, so the device will be calibrated in Section IV A, finding a function mapping voltage to angle and vice versa.

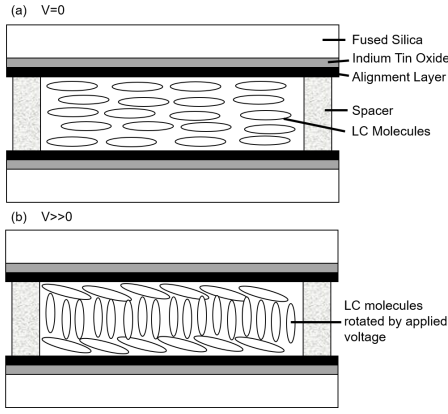


FIG. 6. Schematic of LCVR operation. In (a), no voltage is applied and all molecules in the liquid crystal layer are relaxed and oriented parallel to the outer fused silica and alignment layers. In (b), a voltage $V \gg 0$ is applied and all molecules not pinned to the alignment layer rotate towards a perpendicular orientation, where minimum retardance is achieved.

B. Rubidium Cell

A shielded cylindrical container holds the rubidium cell to avoid interference from non-homogeneous residual fields in the environment. Within this cylinder, three sets of Helmholtz coils (aligned longitudinal to the laser, transverse horizontal, and transverse vertical) form a three-dimensional apparatus to create a magnetic field in any useful direction by adding the axis-aligned magnetic vectors each set of coils produces. Fig. 7 shows the cell enclosure and final photodetector, with a simple lens in between to focus incoming light.

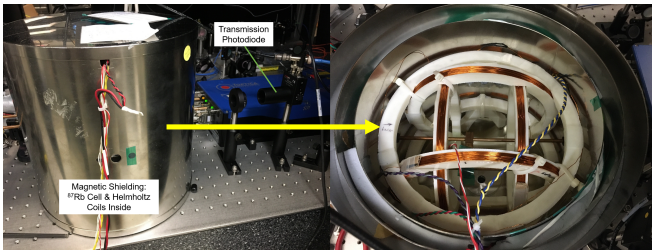


FIG. 7. The shielded ^{87}Rb cell chamber and simple photodetector at the end of the setup. The right image shows the 3D-printed three-dimensional Helmholtz coil setup within.

The cell itself holds only the ^{87}Rb isotope of rubidium and neon buffer gas. Rubidium atoms in the dark state in an EIT resonance tend to lose this superposition state when they collide with the walls of the cell. The atoms have high velocity and can move in any direction, thus many collisions happen per unit time; we do not want our specially-prepared atoms to decay into the ground state rapidly after achieving EIT. The addition of buffer gas is an established trick to alleviate the issue. Rubidium atoms will collide with neon atoms more often and the walls much less, but neon collisions preserve the spin state of rubidium atoms⁶. A part of this exploration is to

Alexander Toyryla

determine the optimal cell parameters. The pressure of buffer gas must be calibrated because too little allows more Rb wall collisions, but too much dulls the effects of EIT transmitted through the cell. Cell temperature is also important and under investigation, because higher temperatures lead to a higher pressure of vaporized ^{87}Rb atoms but less transmitted light.

C. Lock-in Amplifier

A lock-in amplifier is a device that can ensure a signal lock, like on a polarization setting maximizing transmission, by means of finding the first derivative of an input signal. This device can resolve small signals within a great deal of noise so long as it is given the carrier wave of the target signal. It takes in the final photodetector's output signal, a reference signal carrier wave of the same frequency as the output we want, and it outputs what is desired: either an amplified target signal without the noise or a higher derivative of this signal⁷.

In our setup, we want the capability to hold the LCVR polarization at peak or minimum transmission as seen on the curves in Fig. 4. This requires effective dynamic locking of the LCVR input voltage, meaning we need a feedback loop. The derivative of the output signal is a fantastic basis for a feedback loop, since the derivative at any rounded local maximum or minimum is zero. In a sweep around the minimum or maximum, the derivative will look like a steep linear curve through zero with an upward or downward slope respectively. Thus, ensuring the lock-in amplifier's signal is zero ensure we are situated at a transmission peak: this can be used as an error signal for the proportional-integral-derivative (PID) controller, locking the LCVR at a polarization with peak transmission.

D. Auxiliary Electronics and Software

Several additional electronics and computer software are vital for the magnetometer's operation and experimentation that each require a brief mention.

A four-channel oscilloscope is essential for locking the laser, system monitoring, and for most data acquisition. It is connected to a desktop computer such that a MATLAB program can extract any waveform data displayed on the scope screen. Its measurement abilities are common knowledge, but on the topic of locking the laser, the waveform in Fig. 8 is directly viewed on an oscilloscope triggered at the laser's modulation frequency. At this trigger frequency we also see the output of the final photodetector in line with the dichroic atomic vapor laser lock (DAVLL) signal such that the characteristic dips in transmission that occur in the neighborhood of an EIT peak line up with the linear zero-crossing of the DAVLL signal. This helps find the location to lock the laser frequency at before sweeping frequency around the resonance to find EIT peaks.

Frequency sweeps are essential in finding the exact small frequency range where CPT occurs. After laser lock, a Python program on the same desktop computer can perform

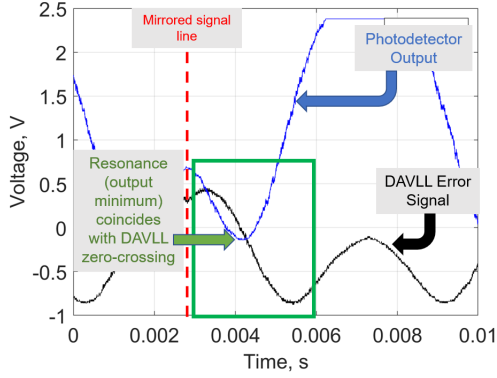


FIG. 8. An example differentiated signal from the DAVLL. Each photodetector detects transmitted light from one of the separated resonances, so when the output signals are subtracted, we end up with a curve as such. The ‘linear’ zero-crossing is where we lock the laser and how the DAVLL detects if we have strayed off resonance. The zero-crossing lines up with the dip in the photodetector output signal where the resonance occurs.

RF sweeps around the central resonance in frequency ranges from 1 Hz to 10 MHz. This is done by precisely modifying the laser input current.

The laser apparatus requires temperature control to achieve rubidium resonance given the small current we supply and the temperature of the main rubidium cell determines its vapor pressure, so two standard temperature controllers are used.

The LCVR that we use pairs with a digital interface controller that ensures a clean and consistent signal is sent to the polarizer. Software pairs with the controller to directly control the input to the LCVR, however in a manner not easily customizable. Instead, we use external input, through this controller, from a function generator. Often we want to use it to set a constant DC offset, sweep through a range of voltages, or to perform high-frequency sinusoidal fluctuations. Two signals of these types can be added together, creating a slow sweeping, a fast modulating, or constant offset signal sent to the LCVR. This signal may be summed with the error signal from the PID controller to lock the LCVR at a polarization with peak transmission.

IV. Results and Discussion

A. LCVR Calibration

The LCVR is a new addition to this ongoing project, so the first task is to find a calibration equation that maps input voltage to angle and vice versa. There are many caveats to this task that make it far more in-depth than it first appears.

The first attempt at a calibration uses the LCVR controller software to control its input voltage. The laser’s temperature controller is switched off so that no rubidium resonances interfere with raw transmission data. A polarizing beam splitter is placed after the LCVR but before the ^{87}Rb cell to observe the change in the LCVR’s effective polarization angle.

Alexander Toyryla

If the LCVR polarizes along the PBS’s polarization axis the full laser intensity will be transmitted, but if it is polarized perpendicularly, no intensity should transmit. The transmitted intensity follows the equation

$$I = I_0 \cos^2 \phi, \quad (1)$$

where I is the transmitted intensity, I_0 is the incident intensity, and ϕ is the relative angle between the polarization axes of the incident light and PBS. Solving Eq. 1 for ϕ and ‘unwrapping’ the results (converting angles to equivalent angles in the cosine function) such that we arrive at a continuous-derivative curve, Figure 9 shows the first calibration result.

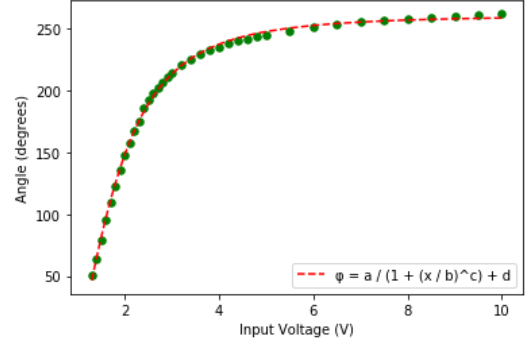


FIG. 9. Input voltage to LCVR angle calibration by stepping to constant voltages and recording photodiode output. In the fit function, $a = -360 \pm 20$, $b = 1.50 \pm 0.06$, $c = 2.72 \pm 0.09$, and $d = 261 \pm 1$. These are statistical uncertainties.

This result is very important: it tells us that voltage does not linearly map to change in angle for the full 0-10 V range. It instead has a best fit function of the form

$$\phi = \frac{a}{1 + (V_{in}/b)^c} + d, \quad (2)$$

which also leads to a function mapping angle to voltage

$$V_{in} = b \left(\frac{a}{\phi - d} - 1 \right)^{1/c}, \quad (3)$$

where a, b, c , and d are fit parameters found every time a calibration is run and V_{in} is the input voltage. Unfortunately, this function becomes less accurate as we reach higher voltages. Fortunately, a full range of 180° occurs before the function loses accuracy: this means we can instead survey a smaller range of voltages to find a better fit function. This choice is made more appealing by the fact that the function’s rate of change at higher voltages is very small; the range of angles covered past 5 V is very small and thus not very useful for this project.

Another important note to make is that the numerical angles listed on the y-axis are calculated relative to the polarization axis of the polarizing beam splitter inserted between the LCVR and rubidium cell. This component is not a permanent part of the setup, meaning these angle numbers are not part of an absolute scale. It is only the relative difference in voltage and the number of degrees travelled from a start point that matters.

We now want to observe the LCVR’s calibration when the voltage is swept rather than individually set to different angles. We used the LCVR controller software to set triangular wave voltage sweeps and recorded the output on an oscilloscope. Since the molecules in the LCVR have a small response time to changes in input voltage, the sweep was varied with three parameters: sweep direction (low to high versus high to low voltage), sweep range (about 1 V about a 90° range versus 10 V), and sweep time (1, 2, 4, 8, and 16 seconds). The results are in Fig. 10.

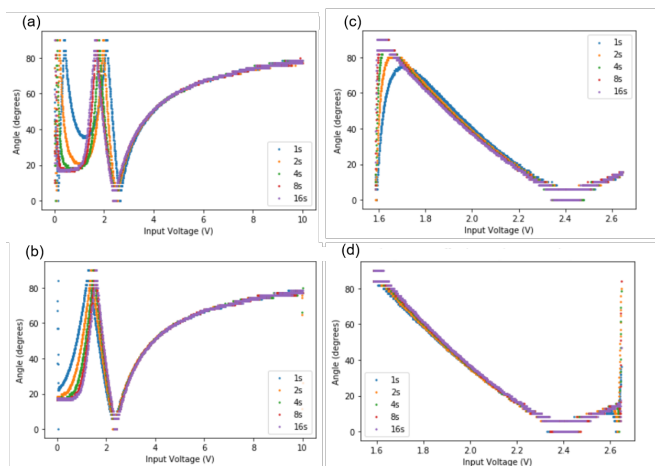


FIG. 10. Input voltage to LCVR angle through twenty different sweep setting combinations. No “unwrapping” is done due to this analysis being qualitative. Sweep time colors are as follows: blue = 1 s, orange = 2 s, green = 4 s, red = 8 s, purple = 16 s. (a) has increasing voltage from 0-10 V, (b) has decreasing voltage from 0-10 V, (c) has increasing voltage from 1.584-2.646 V, and (d) has decreasing voltage from 1.584-2.646 V. The second range is approximately 90° of rotation.

In Fig. 10(a), we have an increasing voltage sweep from 0-10 V. As expected, each of the five sweep times follows the same shape as our initial calibration in Fig. 9, but a clear inconsistency appears in the low voltages: shorter sweeps have a hard time catching up to the angle they should be at when the voltage is swept so fast. The 16 second sweep encapsulates what the sweep should look like best, starting flat and unchanging before 1 V and then changing angle rapidly immediately after. The 1 second sweep (blue) attempts to adjust from 10 V at the end of the last sweep to 0 V, but clearly not fast enough to even reach the 20° starting point it should be at at 0 V. This means it and the other faster sweeps continue to lag behind even on the down-slope starting at 2V. Once the polarization angle starts changing at a slower pace, however, all sweep times have their angles synced to where they should be for the remainder of the voltages.

In Fig. 10(b), the same 0-10 V range is swept, but this time starting at the high 10 V and sweeping down to 0 V. Again, there is inconsistency between the fast and slow sweeps, but this inconsistency is visually smaller. This tells us relaxing the voltage causes a faster reaction from the LC molecules than increasing it.

Fig. 10(c) sees an increasing voltage sweep again but with

a smaller voltage range encapsulating approximately 90° of rotation. This smaller range ensures the sweeps are changing voltage at a slower rate, giving more time for LC molecule reaction. There is certainly more coherence between sweep times in this case versus the same downward slope around 2 V in Fig. 10(a). However, the faster sweeps of 1 and 2 s still lag behind when the sweep starts.

Finally in Fig. 10(d), returning to the better downward sweep but in this smaller range, all sweep times result in an almost immediate shift to the correct angle when the sweep starts on the right. The ‘trace’ points on the right (where the LCVR is rapidly attempting to reach the correct angle) are much more brief than those in Fig. 10(c), and the visual lag behind the 16 s sweep is much smaller. This reinforces the need to sweep from high to low voltage going forward, in a small range if possible, and for longer times.

With this information, a more definitive calibration curve is possible. We now know a decreasing voltage sweep is ideal, slower sweep speeds are ideal (though long sweeps are unrealistic for the final device), and a narrow voltage range gives sweeps more accuracy. This next sweep is 4 seconds long, as it is a realistic time scale while being long enough to achieve a high degree of volt-to-angle accuracy. It takes the range of 3 V between 1 V and 4 V, as this encapsulates more than 180° of rotation and avoids less-useful higher voltages.

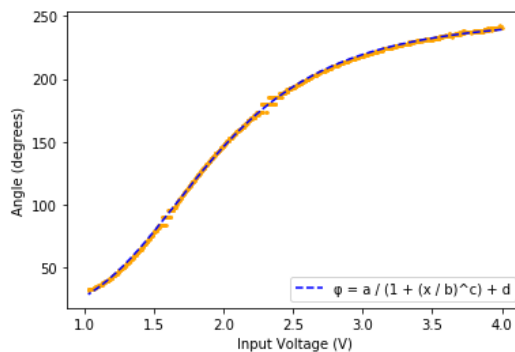


FIG. 11. Input voltage to LCVR angle achieved through a decreasing voltage sweep from 4 V to 1 V for four seconds. In the fit function, $a = -239.1 \pm 0.4$, $b = 1.868 \pm 0.001$, $c = 4.12 \pm 0.01$, and $d = 249.3 \pm 0.1$. The lack of points around 90° and 180° is due to the nature of the arccos conversion from intensity voltage to angle.

Fig. 11 is the result of the calibration sweep. The points follow a curve that the same function type as in Fig. 9 follow. The primary difference, however, is that the lack of deviating points at large V allows fit parameters which fit the data much better. This is numerically evident from the order-of-magnitude smaller errors on all the fit parameters between Fig. 11 and Fig. 9.

This sweeping calibration method is much faster than taking individual points like in Fig. 9, so every time a new voltage source or form of signal modulation was introduced, we ran a calibration sweep to check the same function fit.

B. Applying Modulation

The lock-in amplifier requires a signal with amplitude modulation as input, so the next order of business is to test how the LCVR responds to an input signal with fast modulating amplitude. First, we found in Section IV A that the LCVR has a nontrivial response time to a new applied voltage, so it is reasonable to guess that modulating voltage a large amount with high frequency will result in the device lagging. It will be unable to achieve the full range of rotation for each period of the fast modulating signal.

To test this, we choose four DC offsets for the fast modulating signal and calculate the peak-to-peak modulation amplitude that would cause about $\pm 5^\circ$ of rotation about each DC offset. We place a half-wave plate and PBS after the LCVR and turn off the laser’s temperature control to ensure no EIT interaction. The half-wave plate is rotated to the point where about half of the maximum intensity output is achieved at each DC offset; this is to ensure the modulation of angle achieves the maximum intensity difference when rotated in a 10° range. We disconnect the LCVR’s controller from the controller software and start using a more versatile function generator for the LCVR. We record the peak-to-peak amplitude of the photodetector’s output signal when this modulation signal’s frequency is set to several frequencies.

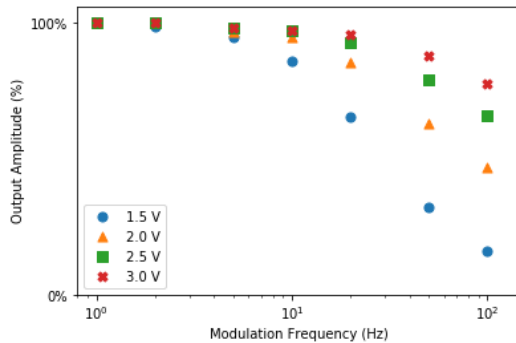


FIG. 12. Effect of increasing modulation frequency on the peak-to-peak amplitude of the photodetector output signal.

In Fig. 12, we achieve what was expected: increasing the frequency of the modulation input decreases the effective rotation range achieved. The more interesting result here is that a higher DC offset for modulation means the overall loss of amplitude is decreased. When at a DC offset of 1.5 V, frequencies not far above 100 Hz cause too significant a loss for the modulation to be useful, falling lower in amplitude than noise. However, working with larger DC offsets allows higher usable frequencies because the loss isn’t as destructive.

An additional reason to use smaller frequencies is that the output signal is distorted and no longer sinusoidal above about 50 Hz. This is traced back to the response time: increasing the voltage to the LCVR shifts its molecules into position quicker than decreasing the voltage, and thus modulation shoots transmission fast in one direction and slow in the other. As a result, we decide to use a modulation frequency of 18 Hz. The lock-in amplifier can pick it up, it is sufficiently small to produce

an easily detectable peak-to-peak amplitude, and no distortion occurs.

C. EIT Peak Frequencies

For many experiments in this work the magnetic field magnitude is held at constant magnitude and transverse ($\theta = 90^\circ$) for maximum output amplitude. This corresponds to inducing a 500 mG field through the set of Helmholtz coils parallel to the ground and transverse to the laser field. The frequency separation of EIT peaks is constant under this condition, as determined by the theory in Section II B, thus it is important to know the exact frequency each peak sits at with this field.

Any half-wave plate or PBS between the LCVR and the cell is removed, the laser temperature control is switched on, and the laser is locked at 6.834 GHz. The RF sweeping Python program is used to change the laser’s frequency with ease and precision.

The lock-in amplifier finds the derivative of the photodiode output, so determining where the lock-in output crosses zero tells us where the peak position is. Unfortunately, experimentation with the lock-in output has the zero-crossing shifted a few kHz from the photodiode output’s EIT peak, as seen in Fig. 13, due to a slow device response time.

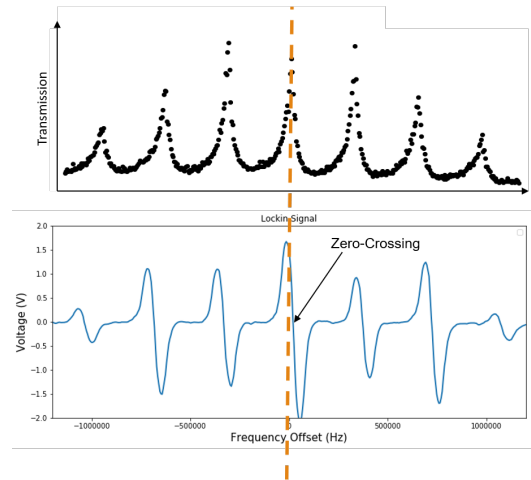


FIG. 13. The lock-in amplifier’s first derivative signal zero-crossing does not align with the EIT transmission peak during testing.

However, switching the lock-in’s setting to measuring the second harmonic of the signal manages to fix this issue. The second harmonic instead finds the second derivative of the input, meaning the EIT peak will not align with a zero-crossing, but instead with a minimum or maximum due to the zero-crossing having a large slope. By first sweeping RF frequencies in a large enough range (± 1.25 MHz) to see all seven EIT peaks and then “zooming in” by sweeping a small (± 5 kHz) range around a peak position, lock-in output data gives a large positive peak with a maximum at the EIT resonance.

Table I displays the frequencies of the EIT resonances at this field strength. Nontrivial noise existed in the lock-in second harmonic signal, so the exact location of the peak was

Resonance	Frequency ($\pm 2 \times 10^{-6}$ GHz)	Δ from $m = 0$ (MHz)
-3	6.8336367	-1.0445
-2	6.8339844	-0.6968
-1	6.8343325	-0.3487
0	6.8346812	0
+1	6.8350323	0.3511
+2	6.8353805	0.6993
+3	6.8357316	1.0504

TABLE I. EIT resonance frequencies for a 500 mG transverse field. The difference from the central resonance is listed in the third column.

found through curve fitting and warrants significant uncertainty. One tip that this data is imperfect (though a useful guide nonetheless) is that the magnitude of the difference from the central resonance for the peaks $\pm 1, \pm 2$, and ± 3 do not each match. It is arguable that parallel magnitudes here fall into each others' uncertainty ranges, but there are certainly methods to decrease the noise in the lock-in signal and achieve more accurate frequency measurements. Accuracy here leads to more accurate measurements of the scalar magnetic field.

D. Magneto-Optical Rotation Caused by Rubidium

We discovered that the effect of magneto-optical polarization rotation had a bearing on our system, gradually rotating the laser's polarization through the rubidium cell. Since we want to achieve a polarization locking mechanism so as to hold our LCVR at the polarization with maximal transmission, we need to characterize this effect so it can be accounted for in future measurements.

This is where the difference signal on the four-channel photodiode is useful: we can measure how the signal moves above or below its off-EIT-resonance zero point, indicating the polarization has rotated. The PBS splitting the post-cell signal into its horizontal and vertical polarization vector components enables the difference measurement.

First, we observe this polarization shift effect on the $m = +2$ resonance over a 180° range of field rotation in θ , from parallel to the laser wave-vector to anti-parallel. We achieve this range by flipping the longitudinal Helmholtz coil input wires, creating a field in the opposite direction while still manipulating the transverse coils to reach any angle desired.

Figure 14 shows us that fields closer to parallel to \vec{k} and fields closer to antiparallel to \vec{k} rotate the laser's polarization in opposite directions. This may give a reliable method to differentiate between supplementary θ angles, like 50° and 130° .

We attempted the same measurements by flipping the transverse field coils in a 180° range. Unfortunately, there was no reliable difference between supplementary angles in this range and thus there is no useful method to find here. We expected this result, however, as we can imagine the polarization shift "peak" in Figure 14 oscillating in amplitude like a cosine wave: the wave crosses zero amplitude at 90° and hits max-

Alexander Toyryla

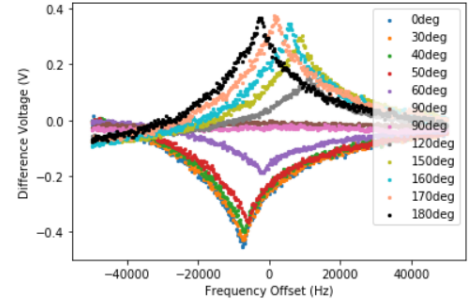


FIG. 14. The differential photodiode's measurements of the rubidium cell's rotation of polarization at different field θ angles for the $m = +2$ resonance. There are two traces at 90° to show no difference between the angle when dialed with flipped coils.

ima and minima at 0° and 180° , so we cannot tell if we are at -10° or 10° by looking at amplitude alone.

Now, we would like to observe if this effect occurs for all the EIT peaks, taking full seven-resonance polarization difference traces at many field angles.

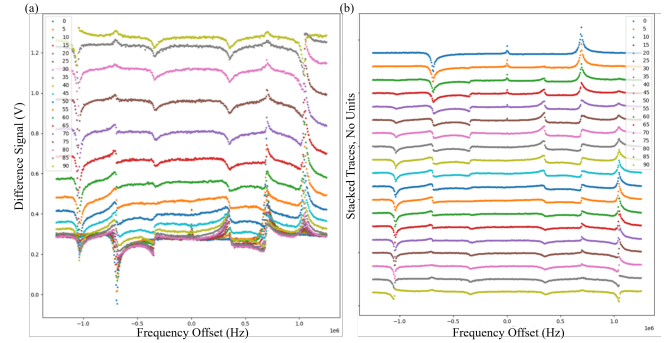


FIG. 15. The differential photodiode's measurements of the rubidium cell's rotation of polarization at different field θ angles over the EIT spectrum range. Each trace has seven deviations from its unique "zero" level, each where an EIT peak normally occurs. Figure (a) is the data at its natural shifting offset (investigated subsequently) and figure (b) is a plot of each trace separated for visual clarity.

Figure 15(b) shows each of these traces stacked on top each other, from $\theta = 0^\circ$ to $\theta = 90^\circ$, clearly showing that at each of the EIT resonant frequencies, a polarization shift occurs. The magnitude of this shift is dependent on the peak and field angle. Mirrored peaks ($m = \pm 2$ for example), have shifts in opposite directions, but of the same magnitude.

Figure 15(a) is initially confusing to look at, since many traces are bunched at the bottom. We expect this when overlaying all traces onto one graph, however, so the strange parts are the traces at higher difference voltages. This indicates that there is another source of self-polarization rotation with changing field angle. As the field moves farther from the laser vector, the background rotation (even off EIT resonances) rotates significantly. We suspect that it could be due to the larger rubidium resonance we are locked onto. Without locking the laser, we observed the entire absorption resonance at a range of field angles.

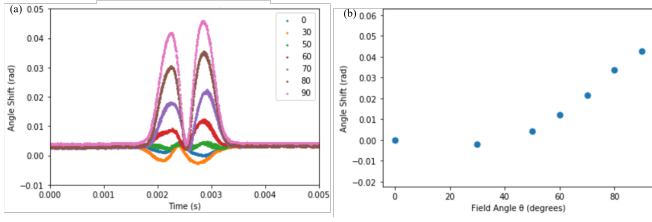


FIG. 16. The differential photodiode’s measurements of the rubidium cell’s rotation of polarization at different field θ angles for the full absorption resonance we lock to. The rightmost difference peak in (a) is our resonance, however the left peak acts in a similar way. (b) tracks the resonance’s difference amplitude and plots how the polarization angle shifts as the field angle changes.

Figure 16 displays how the full absorption resonance shifts the polarization dependent on θ . The rightmost difference peak in Fig. 16(a) is the location of the resonance we lock to; the leftmost peak is a nearby resonance we don’t interact with that acts in a very similar way dependent on field angle. Figure 16(b) tracks the top of the resonance peak for visual clarity as we move through θ angles. There is a clear short rotation in one direction before rotating significantly in the other as we approach $\theta = 90^\circ$. It is important that this data is recorded as this shift needs to be taken into account when calibrating laser polarization-dependent methods for determining magnetic field angle. Without subtracting shifts like this, field direction measurements can be up to 0.05 radians off (about 2.9°), defeating the goals of accuracy this device requires.

E. Establishing a Polarization Lock

We now focus on building a feedback loop by incorporating a summing circuit and a proportional-integral-derivative (PID) controller with input from the lock-in amplifier. The PID controller uses the absolute error from zero, information about the error over time, and the trajectory of the error for the future to rapidly output a voltage that is the difference between the LCVR’s current voltage and that which would bring it to the transmission peak. We sum the hard-set function generator voltage and the PID voltage and apply the sum to the LCVR. The result is, when pre-set within a generous range of the polarization peak, the LCVR is locked to the rotation of maximum output.

There are a few key effects of the lock. First, it does some work to correct noise and imperfections in the LCVR. Though it is not perfect in this regard, this noise has not been a major issue. Second, if we manually change the raw LCVR input on the function generator, the lock will ensure the sum of the new input and the error signal is the same as it was before changing it. Third, to be subsequently tested, the lock should correct the LCVR polarization when the azimuthal ϕ angle is changed with the magnetic field coils rather than the LCVR.

While the difference output on the post-cell photodetector can indicate how much the light’s polarization has rotated, Section IV D gives reason to doubt its efficacy. Figure 17

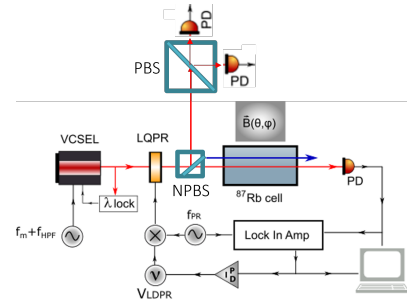


FIG. 17. Location of the pre-cell differential photodiodes in the experimental setup. NPBS stands for non-polarizing beam splitter, which simply diverts some of the laser intensity to the detector’s branch without discriminating based on polarization.

shows the position of the new pre-cell photodetector that calculates the difference between its two photodiodes just like the post-cell detector, but this one is not affected by magneto-optical rotation or other effects that will throw off measurements.

To test the lock’s response to changing field, we use the equation

$$\phi \approx \frac{1}{2} \left(\frac{\Delta I}{\Sigma I} \right) \quad (4)$$

to calculate the angle the polarization has rotated. ϕ is the angle in radians, ΔI is the difference between the intensities measured by each of the balanced photodetectors in either the pre- or post-cell setup (effectively the output of the difference signal), and ΣI is the sum of the two photodetector intensities. The sum is easily measured on the post-cell detector, but for the simplistic pre-cell detector we must rotate the half-wave plate to make the difference zero and cover one detector. We can double the output to find the sum. The reason for the approximation is that the exact equation is $\phi = (1/2)\arcsin(\Delta I/\Sigma I)$, but arcsine is near linear for a significant domain around zero.

The polarization lock is set at $\phi = 90^\circ$ and left active with only this initial setting. 100 second traces of both detector difference and sum signals are taken at field angles $\theta = 90^\circ, \phi = 90^\circ, 88^\circ, 86^\circ, 84^\circ, 82^\circ, 80^\circ$. These are averaged and plugged into equation 4. The average difference between angles measured by the pre-cell detector was $2.05^\circ \pm 0.06^\circ$. This result assures that the feedback loop sets the LCVR to the correct angle to maintain a 90° angle with the magnetic field.

On the other hand, the post-cell detector consistently reads the angle shift much larger than it should have. In this run, we calculated about 4.32° of rotation on average. There are certainly effects like that in section IV D which affect polarization readings after the rubidium cell, and thus we must rule it out as a viable candidate to report on polarization.

Next we must observe the lock’s effectiveness when the θ angle shifts closer to 0, where the field \vec{B} is parallel to the laser vector \vec{k} . In theory, it should start performing worse when closer, as the polarization-induced peak becomes flatter like

in Fig. 4(b). This gives the lock much less information as to where maximum transmission occurs, especially given any noise present.

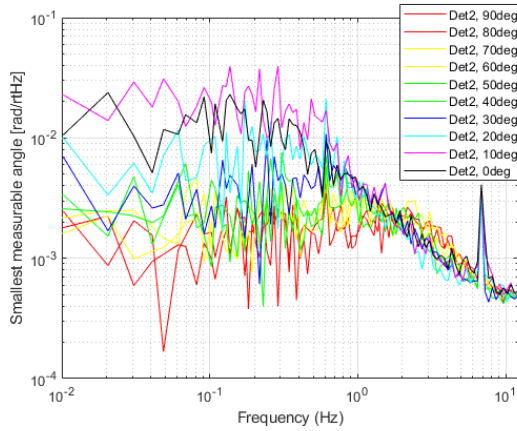


FIG. 18. Fourier transform frequency-noise analysis of the pre-cell detector (Det2) as θ decreases from 90° to 0° , longitudinal with the laser.

Figure 18 shows the results from taking a trace of the pre-cell detector at field angles between perpendicular (90°) to parallel (0°) with the laser vector. There is a very clear increase in the smallest measurable angle as the field moves towards 0° , indicating a large loss in sensitivity. In angles closer to 0° , the detector's difference signal moved dramatically up and down as the locking mechanism struggled to find the exact angle to lock to. This result shows that, using this locking mechanism, the magnetometer will need to measure ϕ ideally when at or closer to $\theta = 90^\circ$.

V. Conclusions

Our role in the first year of this four-year project was a success. We successfully built, tuned, and modified the vector atomic magnetometer to be a fantastic baseline for subsequent researchers to refine precision and automate the process of magnetic field vector measurement.

Installing and calibrating the Liquid Crystal Variable Retarder enabled fast, precise control of the field's apparent azimuthal angle ϕ both manually and under a feedback-driven polarization locking scheme. Observing the system's response to added quick polarization modulation allowed the employment of the lock-in amplifier, critical for the polarization locking feedback loop. Establishing the frequencies we find EIT peaks at under a known field strength informs the calibration of field coil inputs to create angular fields and ensures easy hopping between peaks. Recording the effect of magneto-optical polarization rotation at EIT peaks and on the overall resonance under different field angles informs future calculations and measurement algorithms and provides a simple method for distinguishing fields at supplementary angles. Es-

tablishing a functional polarization locking mechanism fulfills a vital function this device requires to measure the direction of magnetic fields.

Future work to make this magnetometer precise, autonomous, and smaller is already underway. The research described herein is vital to prove the magnetometer's concept and provide a working prototype to those who will make this chip-sized vector atomic magnetometer possible.

Acknowledgments

I first want to thank the Virginia Space Grant Consortium for their generous support through the Undergraduate STEM Research Scholarship Program. I would like to thank the entire William & Mary Quantum Optics group for enthralling presentations and conversations about their research, essential equipment, and navigating the future. I want to thank Dr. Mario Gonzalez Maldonado for his excellent differential photodetector and Tyler Hutchison for the 3-D printed three-dimension Helmholtz coils. My sincerest thanks go to Dr. Novikova and Dr. Mikhailov, who took me on as an honors student at the last second in the midst of an administrative crisis and gave undying support and direction through the entire year.

- ¹A. Edelstein, en“Advances in magnetometry,” **19**, 165217 (2007), publisher: IOP Publishing.
- ²C. J. Cochrane, J. Blacksberg, M. A. Anders, and P. M. Lenahan, en“Vectorized magnetometer for space applications using electrical readout of atomic scale defects in silicon carbide,” *Sci Rep* **6**, 37077 (2016).
- ³K. Cox, V. I. Yudin, A. V. Taichenachev, I. Novikova, and E. E. Mikhailov, “Measurements of the magnetic field vector using multiple electromagnetically induced transparency resonances in Rb vapor,” *Phys. Rev. A* **83**, 015801 (2011), publisher: American Physical Society.
- ⁴O. Gravrand, A. Khokhlov, J. L. Le Mouël, and J. M. Léger, “On the calibration of a vectorial 4He pumped magnetometer,” *Earth, Planets and Space* **53**, 949–958 (2001).
- ⁵W. Happer and H. Tang, “Spin-Exchange Shift and Narrowing of Magnetic Resonance Lines in Optically Pumped Alkali Vapors,” *Phys. Rev. Lett.* **31**, 273–276 (1973), publisher: American Physical Society.
- ⁶S. Brandt, A. Nagel, R. Wynands, and D. Meschede, “Buffer-gas-induced linewidth reduction of coherent dark resonances to below 50 Hz,” *Phys. Rev. A* **56** (1997), 10.1103/PhysRevA.56.R1063.
- ⁷C. Svetlo, G. Galzerano, E. Bava, F. Ferrario, A. Arie, R. Klein, M. Arbore, M. Fejer, A. Onae, and M. Marano, “High-resolution spectroscopy of the 39K transitions at 770 nm and 13C2H2 saturated lines by a solid-state laser at 1.54 m: toward an accurate frequency standard in the optical communication band,” *Instrumentation and Measurement, IEEE Transactions on* **51**, 764–769 (2002).
- ⁸V. I. Yudin, A. V. Taichenachev, Y. O. Dudin, V. L. Velichansky, A. S. Zibrov, and S. A. Zibrov, “Vector magnetometry based on electromagnetically induced transparency in linearly polarized light,” *Phys. Rev. A* **82**, 033807 (2010), publisher: American Physical Society.
- ⁹J. Kitching, “Chip-scale atomic devices,” *Applied Physics Reviews* **5**, 031302 (2018), publisher: American Institute of Physics.
- ¹⁰B. D. Agap'ev, M. B. Gornyi, B. G. Matisov, and Y. V. Rozhdestvenskiĭ, en“Coherent population trapping in quantum systems,” *Phys.-Usp.* **36**, 763 (1993), publisher: IOP Publishing.
- ¹¹L. Essen, E. G. Hope, and D. Sutcliffe, en“Hyperfine Splitting of Rubidium-87,” *Nature* **189**, 298–298 (1961), bandiera_abtest: a Cg_type: Nature Research Journals Number: 4761 Primary_atype: Research Publisher: Nature Publishing Group.
- ¹²N. T. Belcher, en*Development of a Prototype Atomic Clock Based on Coherent Population Trapping*, Thesis, William & Mary (2008).